



## Research article

# MnO<sub>2</sub>-modified ZIF-67 supported on doped reduced graphene oxide as highly active catalyst for the oxygen reduction reaction

S. Fajardo<sup>a</sup>, P. Ocón<sup>b,\*</sup>, A. Arranz<sup>c</sup>, J.L. Rodríguez<sup>a</sup>, E. Pastor<sup>a,\*</sup>

<sup>a</sup> Instituto de Materiales y Nanotecnología, Departamento de Química, Universidad de La Laguna, PO Box 456, 38200, La Laguna, Santa Cruz de Tenerife, Spain

<sup>b</sup> Departamento de Química Física Aplicada, Universidad Autónoma de Madrid, C/Francisco Tomás Valiente 7, 28049, Madrid, Spain

<sup>c</sup> Departamento de Física Aplicada, Universidad Autónoma de Madrid, C/Francisco Tomás y Valiente 7, 28049, Madrid, Spain

## ARTICLE INFO

## Keywords:

Oxygen reduction reaction  
Heteroatom-doped graphene materials  
Zeolitic imidazole framework  
Catalyst

## ABSTRACT

In this investigation, ZIF-67 supported on non-doped reduced graphene oxide (rGO), nitrogen- and sulphur-doped reduced graphene oxide (SN-rGO), and manganese-modified ZIF-67/SN-rGO are synthesized and compared as electrocatalysts for the oxygen reduction reaction (ORR) in alkaline conditions. XPS, SEM, XRD and Raman spectroscopy techniques are used to physiochemically characterize the materials. Cyclic and linear sweep voltammetry unveil kinetic parameters, including rate constants, Tafel slopes, and exchange current density, providing insights into the reaction mechanism. Nitrogen and sulphur doping of graphene reduces hydrogen peroxide production, lowering overpotential and enhancing cathodic currents. Manganese modification further enhances performance, matching cathodic currents with Pt/C and achieving a potential of 0.85 V vs RHE at  $-1 \text{ mA}\cdot\text{cm}^{-2}$  demonstrating superior efficiency. The study highlights the impact of graphene doping and manganese incorporation on ORR activity, contributing to a comprehensive understanding of these electrocatalytic systems.

## 1. Introduction

Sustainable and green energy devices such as fuel cells or metal air batteries are among the most promising strategies to address the global energy and environment challenges caused by heavy reliance upon fossil fuels [1–3]. The oxygen reduction reaction (ORR) is of paramount significance in these types of devices. Currently, the state-of-the-art catalysts are still relied on noble metal-based electrocatalysts due to the low overpotentials and large current densities. However, the scarcity, high cost and chemical susceptibility such as CO poisoning, limit their large-scale production for ORR [4].

In the last decade, carbon-based materials have attracted the attention of numerous researchers due to their properties such as high electric conductivity and large surface area. More concretely, heteroatom doped carbon materials present excellent electrocatalytic activity due to the asymmetrical electron spin density and charge polarization relied on the difference of electronegativity between carbon and the dopant atoms such as B, P, N, S or F [5,6].

In addition, the use of non-noble metal such as Cu, Co or Mn as ORR electrocatalyst have been widely explored due to their low cost and theoretically high catalytic activity [7–9]. Nonetheless, the low chemical stability of cobalt produces the apparition of cobalt oxides which,

despite presenting a great electrocatalytic activity, their intrinsically low conductivity and structural stability results in sluggish ORR kinetics. In order to alleviate these deficiencies, supporting the metal specie on a conductive material such a reduced graphene oxide, not only results in a high stability and catalytic activity but also prevents the agglomeration of the metal particles during their use and creates new ORR active sites [7,8,10,11].

Different cobalt-based metal–organic frameworks (MOF) have been used as precursors for the synthesis of ORR catalyst. Zeolitic imidazole framework-67 (ZIF-67) have demonstrated to be an adequate precursor due to its porous 3-dimensional structure with Co-N bonding, which is reported as a highly active site for que adsorption and reduction of oxygen [12–15]. However, ZIFs are not electrically conductors, making necessary the addition of other conducting materials in order to address the problem [16].

As a result of the efforts for having a high efficiency catalyst, numerous researches have reported the high quality of manganese based materials as catalysts for the ORR [17–19]. More concretely, there are many works in the literature describing the capability of substituting or alloying Co atoms with other transition metals such as Mn for tuning the electronic and electrocatalytic activities of these materials [20–22].

In this study, ZIF-67 was synthesized and immobilized on reduced

\* Corresponding authors.

E-mail addresses: [pilar.ocon@uam.es](mailto:pilar.ocon@uam.es) (P. Ocón), [epastor@ull.edu.es](mailto:epastor@ull.edu.es) (E. Pastor).

graphene oxide (rGO). Through this integration, a catalyst (ZIF/rGO) with enhanced electrical conductivity was prepared by annealing, thus addressing the inherent limitation of MOFs and rendering it suitable for electrochemical investigations. Moreover, to further enhance the catalytic performance, ZIF-67 was supported onto SN-rGO (ZIF/SN-rGO), based on the well-established concept that nitrogen and sulphur doping in graphene structures can effectively improve the activity towards the ORR [23–26]. By comparing the electrochemical responses of ZIF/SN-rGO with ZIF/rGO, the impact of the doping strategy on the ORR performance was elucidated. Additionally, it is explored the modification of ZIF-67/SN-rGO by introducing manganese, aiming to further optimize the electrocatalytic activity.

We emphasize that the novelty of this study lies in unravelling new insights into the ORR mechanism on non-noble metal-based electrocatalysts supported on graphene. Through the comprehensive analysis of the charge transfer coefficient using multiple methods, we have uncovered nuanced details in the electrochemical behaviour. Furthermore, the incorporation of both doped and undoped graphene has resulted in significant and previously unexplored effects on ORR kinetics. These findings contribute to the growing understanding of advanced materials for sustainable electrocatalysis, providing a valuable addition to the existing body of knowledge.

## 2. Experimental

### 2.1. Synthesis of graphene oxide

Graphene oxide was synthesized following the Hummers modified method [27]. In summary, 3.5 g of  $\text{KMnO}_4$  (>99.8 %, Panreac) were slowly added into a 250 mL Erlenmeyer flask containing 30 mL of  $\text{H}_2\text{SO}_4$  (Merck p.a.) and 1 g of graphite (Sigma-Aldrich). Then, the mixture was diluted to 80 mL using ultrapure water (18.2 M  $\Omega$  cm) and stirred for 1 h at 35 °C. After that, the solution was heated up to 95 °C for 15 min and diluted to 200 mL with ultrapure water. Next, 1.25 mL of  $\text{H}_2\text{O}_2$  (30 % v/v, Foret) was slowly added. The solution was stirred for 24 h, and then, centrifuged with ultrapure water until a pH of about 7 was achieved in the supernatant. Finally, the GO was dried at 60 °C in an oven.

### 2.2. Preparation of ZIF-67 and ZIF-TT

For the synthesis of ZIF-67, 2 g of  $\text{Co}(\text{NO}_3)_2$  (99.99 %, Sigma-Aldrich) was dissolved in 100 mL of water to form solution A. On the other hand, 2.2 g of 2-methylimidazole was dissolved in 100 mL of water to form solution B. While solution B is being stirred, solution A was added dropwise, and a purple solution was instantly obtained indicating the formation of the MOF. The obtained solution was stirred for 24 h and then washed by centrifugation at 3000 rpm with ethanol and dried at

60 °C in an oven, obtaining the ZIF-67 as a purple powder.

The obtained solid was thermally treated in a tubular furnace under Ar atmosphere at a flow rate of 100 mL/min. First, a temperature ramp of 2 °C/min was applied up to 200 °C where was kept for 30 min, after this, the same ramp was applied up to 700 °C where was kept for 2 h. The obtained solid was acid leached for 4 h, washed by centrifugation with ethanol and dried at 60 °C in a furnace for 24 h, obtaining the ZIF-TT.

### 2.3. Preparation of ZIF/graphene composites

For the synthesis of ZIF/graphene nanocomposites, the same procedure as for the synthesis of ZIF-67 was followed but adding 100 mg of GO to solution B, obtaining the ZIF/GO material which presents a dark purple colour. Then, the same thermal treatment was carried out, reducing the GO, and producing ZIF/rGO.

To prepare the ZIF/SN-rGO catalyst, ZIF/GO was ground with 100 mg of thiourea and then the same thermal treatment was applied obtaining a black powder (see Fig. 1).

### 2.4. Preparation of MnZIF/SN-rGO

The synthesis of MnZIF/SN-rGO was by the same method used for ZIF/SN-rGO adding 20 mg of manganese acetate ( $\text{Mn}(\text{Ac})_2 \cdot 4\text{H}_2\text{O}$ , 99.0 %, Sigma-Aldrich) to the mixture of  $\text{Co}(\text{NO}_3)_2$ , 2-methylimidazole and GO after being stirred for 30 min.

### 2.5. Physicochemical characterization

X-ray diffraction analysis was performed using a PANalytical X'PERT-Pro diffractometer for powder samples, applying  $\text{Cu-K}\alpha$  radiation ( $\lambda = 0.15406$  nm) at 40 kV and 20 mA.  $2\theta$  values scans were recorded between 5° and 100° at 0.04°  $\text{s}^{-1}$ . The lattice parameters were obtained by refining the unit cell dimensions by the least square method. Interplanar distance and crystallite size were determined applying the standard procedure published by Iwashita et al. [28] using Bragg's law (Eq. (1)) and Debye-Scherrer expressions (Eq. (2)), respectively:

$$2d_{hkl} \cdot \sin \theta = n \cdot \lambda \quad (1)$$

$$L_c = \frac{0.9 \cdot \lambda}{\beta_{1/2} \cdot \cos \theta} \quad (2)$$

where  $d_{hkl}$  is the interplanar distance,  $\theta$  is the scattering angle,  $\lambda$  is the wavelength of the incident wave,  $L_c$  is the crystallite size, and  $\beta_{1/2}$  is the full width at half maximum.

X-ray photoelectron spectroscopy (XPS) spectra were acquired using a hemispherical analyser equipped with five channeltron detectors

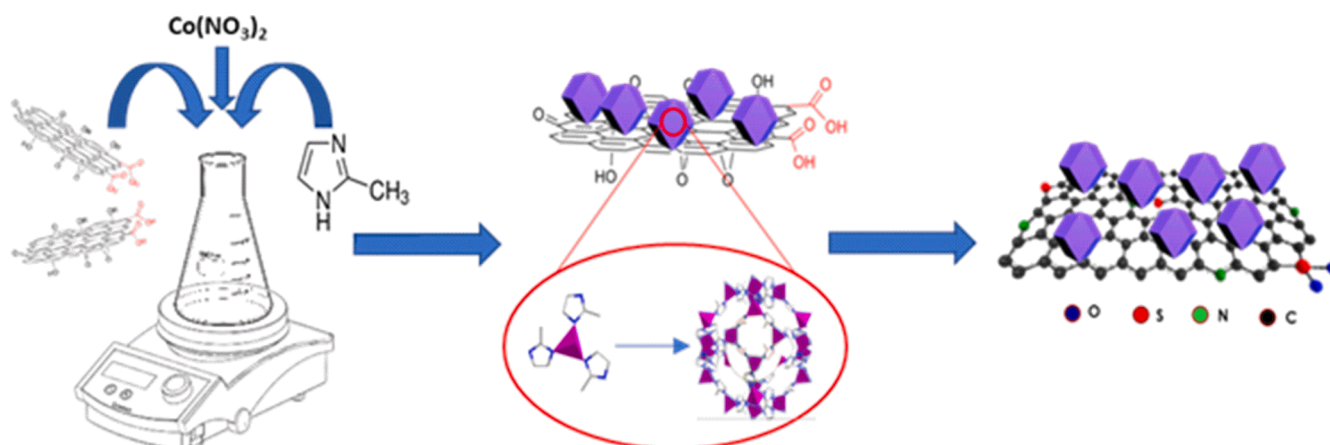


Fig. 1. Synthesis of ZIF/graphene nanocomposites.

(SPECS Phoibos 100 MCD-5). The Al K $\alpha$  radiation ( $h\nu = 1486.6$  eV) of a twin-anode X-ray source operating at 300 W was used. The base pressure in the analysis chamber was below  $1 \cdot 10^{-8}$  mbar during spectra acquisition. Binding energies were determined by referencing the C1s peak of C-C species at 284.5 eV. SEM analysis was performed by using a Tescan Vega 3LMU machine.

Raman spectra were recorded on a Renishaw confocal Raman Microscope spectrometer inVia model with an excitation wavelength of 532 nm. The Raman scattered light was recorded from 100 to 3200  $\text{cm}^{-1}$ . Elemental analysis measurements were performed using an Elemental Analyzer CNHS FLASH EA 1112 (Thermo Scientific). Finally, energy dispersive X-ray analyser (Oxford 6699 ATW, Oxford, Oxfordshire, UK) was used to determine the metal load.

## 2.6. Electrochemical characterization

For the electrochemical measurements an Autolab PGSTAT30 potentiostat–galvanostat (Metrohm Autolab) was used. All the experiments were carried using a three-electrode glass cell at room temperature in 0.5 M  $\text{H}_2\text{SO}_4$  (99.99 %, Sigma Aldrich) electrolyte. A glassy carbon rod was used as counter electrode and a reversible hydrogen electrode (RHE) in the supported electrolyte as reference electrode. A rotating ring-disk electrode (RRDE, PINE) with a glassy carbon disk (disk diameter 5 mm) and a Pt ring (collection efficiency determined to be  $N = 0.22$ ) was used as working electrode. The catalyst inks were prepared by mixing 2 mg of the catalyst with 15  $\mu\text{L}$  of Nafion® perfluorinated solution (5 wt% in a mixture of lower aliphatic alcohols and water) and 500  $\mu\text{L}$  of milli-Q water. Then, 20  $\mu\text{L}$  of the ink were deposited on the glassy carbon disk of the RRDE using a micropipette and dried under nitrogen atmosphere. The total catalyst loading is  $0.4 \text{ mg} \cdot \text{cm}^{-2}$ .

Ar (99.999 %, Alpha GAZ, Air Liquide) was bubbled into the solution during 15 min to deoxygenate the electrolyte. An activation process was applied before the measurements, consisting of performing cyclic voltammetry in the potential range of 0.05–1.00 V at  $0.20 \text{ V} \cdot \text{s}^{-1}$  until a reproducible voltammogram is reached. Then, deoxygenated cyclic voltammograms (CVs) were recorded at different scan rates. Afterwards, the solution was saturated with  $\text{O}_2$  (99.999 %, Alpha GAZ, Air Liquide) by bubbling it during 15 min and the CVs were recorded in the same

conditions. Steady state polarization curves were acquired at 400, 600, 900, 1600 and 2500 rpm in an  $\text{O}_2$  saturated solution. For this, a linear sweep voltammograms (LSVs) were performed from 1 to 0.05 V at  $0.002 \text{ V} \cdot \text{s}^{-1}$ . The Pt ring potential was maintained at 1.2 V during the scans for obtaining the currents generated by the oxidation of the produced  $\text{HO}_2^-$  into  $\text{O}_2$ . Both ring and disk currents ( $I_r$  and  $I_d$ ) were recorded as a function of the disk electrode potential.

The average number of transferred electrons during the ORR, as well as the percentage of  $\text{H}_2\text{O}_2$  produced, were determined by the following equations (Eqs. (3) and (4), respectively):

$$n = \frac{4 \cdot J_d}{J_d + J_r/N} \quad (3)$$

$$\% \text{H}_2\text{O}_2 = \frac{200 \cdot J_r/N}{J_d + J_r/N} \quad (4)$$

where  $J_d$  is the current density generated at the disk,  $J_r$  is the ring current density produced at the ring, and  $N$  is the current collection efficiency of the Pt ring.

## 3. Results and discussion

### 3.1. Physicochemical characterization

The analysis of the morphology and composition of the studied materials was carried out using the SEM-EDX technique, which was useful for determining the content of metallic species. As seen in Fig. 2a, ZIF-67 forms the usual hexagonal nanoparticles (NPs) reported in the literature for this type of MOF material [7,29], besides, there are some NPs that do not present this structure, indicating that in some cases the growth was not completed. The diameter of these NPs oscillates between 500 and 600 nm. After the heat treatment, it seems that the walls collapse, giving rise to a concave curvature, leaving the edges more exposed; furthermore, NPs merge, producing a macrostructure in which the hexagonal shape of the NPs is visible (Fig. 2d). In the case of ZIF/GO (Fig. 2b), a smaller and smoother hexagonal structure with a diameter ranging from 100 and 300 nm is observed, indicating that the presence

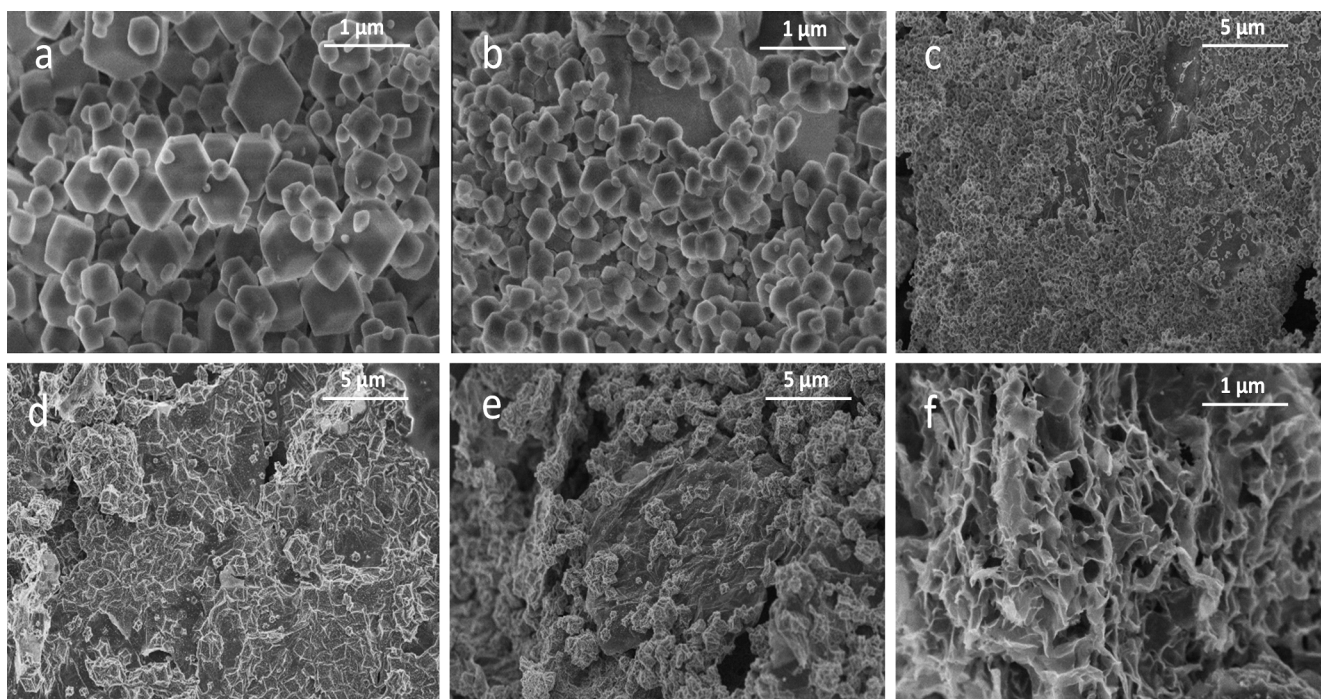


Fig. 2. High resolution SEM images for: a) ZIF-67, b) ZIF/GO, c) ZIF/SN-rGO, d) ZIF-TT, e) ZIF/rGO, and f) MnZIF/SN-rGO.



of GO interferes with the growth of the ZIF crystal. In the same way as ZIF-67, when ZIF/GO is subjected to heat treatment, the structure of the nanoparticles collapses; however, in this case, the agglomeration on the rGO sheet is lower, which may result in a larger electroactive surface area (Fig. 2e). A similar morphology is observed for ZIF/SN-rGO (Fig. 2c) while for MnZIF/SN-rGO it is quite different, resulting in a totally amorphous structure (Fig. 2f). The at. % of metal load in the catalyst was determined by EDX by mapping five different points of each sample. It should be noted that while EDX is a valuable technique for elemental analysis, its quantification capabilities may be limited by the geometry of the samples, thus, it may not provide precise composition data. Nonetheless, the obtained results still offer valuable elemental composition information. Results indicated 4.2 and 11.0 at. % of Mn and Co, respectively, for Mn/SN-rGO, and  $\sim 4.5$  at. % of Co for the other ZIF/graphene composite catalysts. The Co content in MnZIF/SN-rGO results to be higher than for ZIF/rGO and ZIF/SN-rGO, which could suggest the formation of other chemical species from Co during the synthesis, e.g. cobalt oxide, apart from the Co incorporated into MnZIF/SN-rGO as ZIF-67. This assumption agrees with XPS analysis, which shows a Co3+ contribution only in Co 2p spectrum of MnZIF/SN-rGO (see later).

Aiming to determine the presence of N and S in the catalysts, elemental analysis measurements were carried out and the results are summarized in Table S1. Since elemental analysis cannot determine metallic species, it was limited to establish the presence of nitrogen and sulphur in the synthesized materials. It must be taken in mind that in these values, the percentage of Mn and Co is shown together with that of O (as it is commonly assumed that the weight that does not belong to C, H, N or S is only due to the later). Even so, it is still a useful test to compare the content of the other elements in the different samples.

According to Table S1, ZIF-TT is the material that presents the lowest C content (0.82 % wt.). However, when mixing the MOF with the graphene materials, a large increase in carbon content is observed, which decreases again in the MnZIF/SN-rGO because Mn contributes to the weight of the sample. N appears in all materials due to ZIF-67 but is found in higher proportion in ZIF/SN-rGO and MnZIF/SN-rGO due to its content in SN-rGO. On the other hand, elemental analysis measurements show the presence of S in all the samples, in a higher proportion in the

materials prepared with doped graphene (S in ZIF-TT and ZIF/rGO can be explained as impurity from the  $\text{H}_2\text{SO}_4$  used in the GO synthesis).

The structure and crystallinity of the catalysts were established from XRD and Raman spectroscopy measurements (Fig. 3a and 3b).

Raman spectra are similar for the different materials, except for ZIF-TT, which does not show any signal corresponding to the D and G bands located at  $1340$  and  $1586\text{ cm}^{-1}$  as they are associated with  $\text{sp}^3$  and  $\text{sp}^2$  carbon domains, respectively. The relation between the intensities of the D and G bands ( $I_D/I_G$ ) is often used to have a qualitative idea of the structural disorder degree in carbonaceous materials [30]. The disorder degree in this type of materials is directly related to the electrocatalytic activity towards the ORR [30,31].  $I_D/I_G$  values increases in the materials in the following order: ZIF/rGO (1.03) < ZIF/SN-rGO (1.05) < MnZIF/SN-rGO (1.14). This is in accordance with Section 5.2 where it is shown the same sequence for increasing the electrocatalytic activity towards the ORR.

In addition, two main bands at  $415$  and  $670\text{ cm}^{-1}$  are distinguished for ZIF/rGO, ZIF/SN-rGO and MnZIF/SN-rGO. The band at  $415\text{ cm}^{-1}$  corresponds to the Co-N bond while the one at  $670\text{ cm}^{-1}$  is the vibrational mode of the 2-methylimidazole ligand. A fifth band can be distinguished in MnZIF/SN-rGO at  $644\text{ cm}^{-1}$  which is usually associated with  $\text{MnO}_2$  [32].

XRD pattern of ZIF-TT perfectly matches with the simulated spectra of ZIF-67 (see Figure S1) [9,13], suggesting that the thermal treatment does not modify the crystalline structure of this material. On the other hand, the XRD patterns of graphene nanocomposites show three main peaks. The first one located at  $26^\circ$  is related to (002) diffraction plane of graphite, while the peaks located at  $44^\circ$ ,  $51^\circ$  and  $76^\circ$  are associated to Co(111) and Co(200) of crystalline Co [9,33]. A wide band is observed at lower  $2\theta$ , below the (002) plane of graphite, which can be related to the amorphization of the catalyst [34].

Different parameters were obtained for graphene-based catalysts from XRD diffractograms and summarized in Table 1. An approximation of the graphene layers that make up graphene materials can be obtained by dividing the crystallite size by the interplanar distance (Table 1). The estimated number of layers increases in the subsequent way: MnZIF/SN-rGO (6) < ZIF/SN-rGO (6) < ZIF/rGO (11). A smaller number of layers leads to a higher surface area in graphene materials increasing the

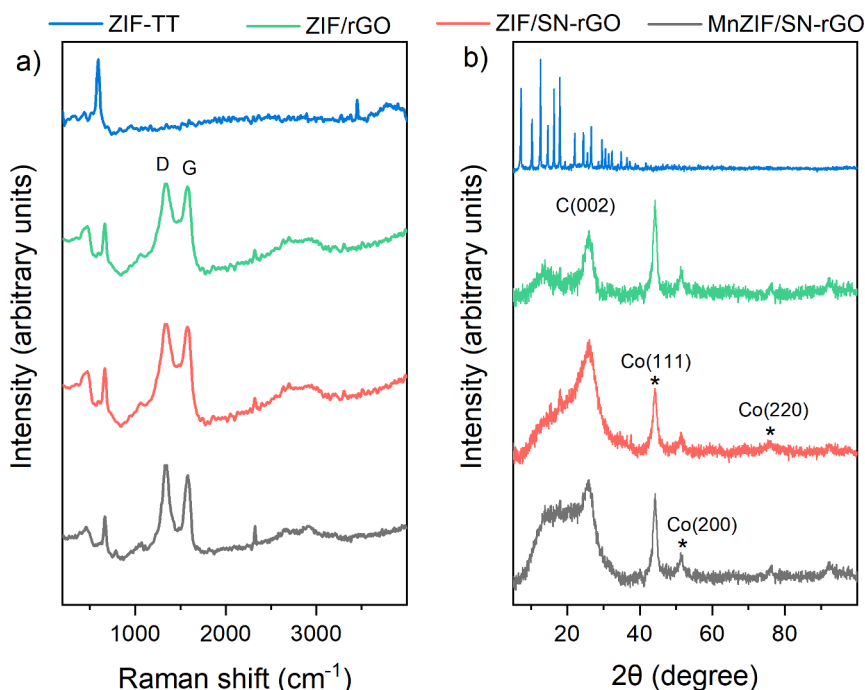


Fig. 3. Raman spectra (a) and XRD (b) of the studied catalysts (ZIF-TT, ZIF/rGO, AIF/SN-rGO and MnZIF/SN-rGO).

**Table 1**  
Crystallographic parameters obtained from XRD spectra.

Material	2 $\theta$ (0 0 2) / degree	Interplanar distance (d) / nm	Crystallite size ( $L_c$ ) / nm	Number of layers	$I_p/I_g$
Zif/rGO	26	0.35	8.2	11	1.03
Zif/SN- rGO	24	0.37	1.8	6	1.06
MnZIF/ SN-rGO	24.7	0.36	1.7	6	1.14

presence of edge sites, which could lead to higher current densities during the ORR [27,35]. This agrees with the results in Section 3.2 where limiting current densities increase inversely proportional to the number of layers.

MnZIF/SN-rGO and ZIF/SN-rGO Co 2p XPS spectra are given in Fig. 4 after background subtraction based on the Tougaard method [36]. Attending to Co 2p spectrum, two main peaks associated with Co 2p<sub>3/2</sub> and Co 2p<sub>1/2</sub> core levels are observed at 780.6 and 796.2 eV, respectively, in the case of MnZIF/SN-rGO, whereas they appear at 780.8 and 796.4 eV for ZIF/SN-rGO [37,38]. For the determination of the cobalt state, it is generally used the energy separation between the Co 2p<sub>3/2</sub> peak and its corresponding satellite. This separation is reported to be ~ 6.0 eV for Co<sup>2+</sup> cation, while for the Co<sup>3+</sup> cation typically an energy separation of ~ 10 eV has been found [37,38]. In the case of MnZIF/SN-rGO, two satellite peaks associated with the Co 2p<sub>3/2</sub> peak are observed at 786.1 and 790.6 eV. The energy separation between these satellites and the Co 2p<sub>3/2</sub> peak is 5.3 and 9.8 eV, respectively, therefore suggesting the presence of both Co<sup>2+</sup> and Co<sup>3+</sup> species. On the other hand, only one satellite peak related to the Co 2p<sub>3/2</sub> core level was observed for ZIF/SN-rGO at 786.1 eV, with an energy separation of 5.5 eV with respect to the Co 2p<sub>3/2</sub> peak, thus in this case only Co<sup>2+</sup> species seems to be present. Co 2p<sub>3/2</sub> and 2p<sub>1/2</sub> of MnZIF/SN-rGO were deconvoluted using two peaks associated with Co<sup>2+</sup> and Co<sup>3+</sup> species, respectively, as shown in Fig. 4. In the case of ZIF/SN-rGO, an additional fitting peak than that found for Co<sup>2+</sup> species is necessary at lower binding energies to perfectly reproduce the overall shape of the Co 2p core level. This additional species can be related to the presence of metallic cobalt, Co<sup>0</sup> [15,18,39,40].

The addition of Mn to the catalyst seems to favour the insertion of oxygen in the structure which can lead to the formation of Co<sub>3</sub>O<sub>4</sub> explaining the presence of Co<sup>3+</sup> in XPS spectrum of MnZIF/SN-rGO.

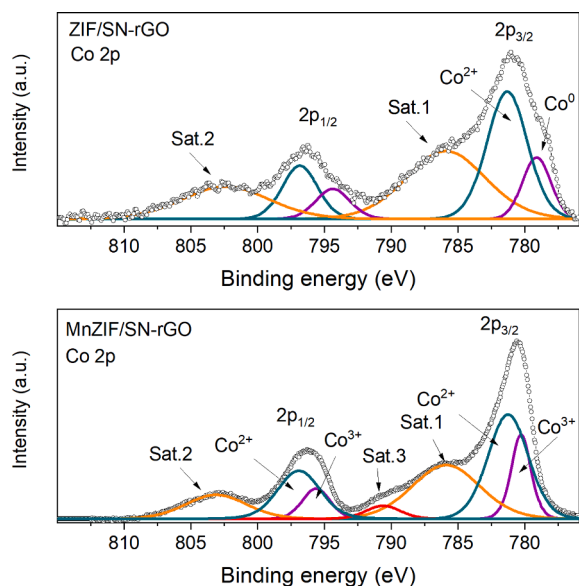


**Fig. 4.** Co 2p spectra of ZIF/SN-rGO (top) and MnZIF/SN-rGO (bottom).

These species also justify the higher electrocatalyst activity of this material compared to the others [41]. Co<sub>3</sub>O<sub>4</sub> is reported in the literature as a highly active catalyst towards the ORR and, although the mechanism at this oxide remains unclear, different assumptions have been made. For example, Xu et al. [42] reported that exposing Co<sup>3+</sup> on the surface of the catalyst can lead to an enhancement kinetics of the ORR. The O1s spectrum of MnZIF/SN-rGO (see Figure S1) supports this fact, with a higher contribution of M–O (M = Co or Mn) at 529.8 eV with respect to the other catalysts.

In addition, Mn 2p spectrum reveals three peaks located at 642.4, 654.0 and 665.0 eV associated with Mn 2p<sub>3/2</sub> and 2p<sub>1/2</sub> core levels and the Mn 2p<sub>1/2</sub> corresponding satellite peak, respectively (Table S2 and Figure S3). The energy difference between the Mn 2p<sub>1/2</sub> core level and its corresponding satellite peak, termed as  $\Delta 2p_{1/2}$  in the literature, is commonly used for determining the oxidation state of Mn [17]. The resulting  $\Delta 2p_{1/2}$  was 11 eV, therefore suggesting the formation of MnO<sub>2</sub> species. In addition, the binding energy of the Mn 2p<sub>3/2</sub> core level peak is also in good agreement with the values reported for MnO<sub>2</sub> [17,43]. Risch et al. [44,45] reported that Mn<sup>4+</sup> species are active catalyst for the ORR. Furthermore, the addition of other metals with valences like cobalt species in ZIF-67, helps enhancing the overall ORR activity by stabilizing MnO<sub>x</sub> species [46], which could explain the high electrocatalytic activity obtained in the present paper for MnZIF/SN-rGO towards ORR in next sections.

The XPS spectra of N1s and C1s were also analysed according to the literature [37,38,47–49] and the peak information is given in the supplementary material (Table S2).

### 3.2. Evaluation of the electrocatalytic activity

The LSVs were recorded at different rotating speeds for the evaluation of the electrocatalytic activity of the catalysts towards the ORR (Figure S4). These curves show a different behaviour depending on the catalyst (Fig. 5). First, ZIF-TT and ZIF/rGO are the materials that develop the lower current densities and an enhancement in the limiting current density ( $j_L$ ) is observed when ZIF-TT is mixed with the different graphene materials. ZIF/rGO displays an increase in  $j_L$  of around 0.7

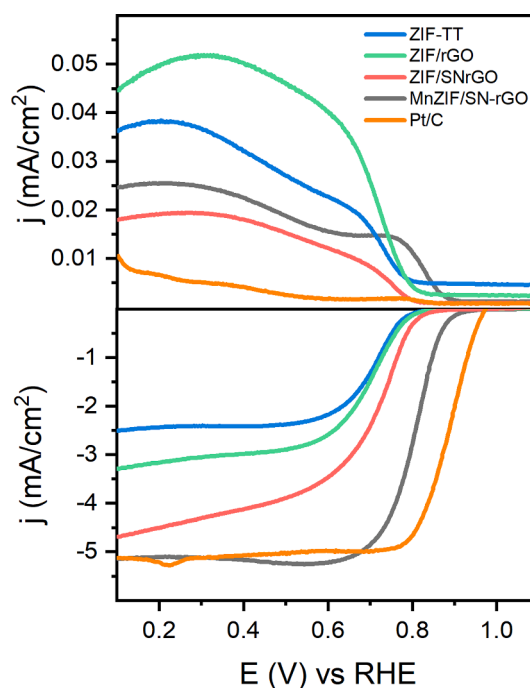


**Fig. 5.** Ring (top) and disk (bottom) current densities recorded during LSV measurements at 1600 rpm, 2 mV s<sup>-1</sup> in H<sub>2</sub>SO<sub>4</sub> 0.5 M, O<sub>2</sub> saturated medium.

$\text{mA}\cdot\text{cm}^{-2}$  compared with ZIF-TT. However, it should be noted that the hydrogen peroxide currents recorded at the ring also increase. In the case of ZIF/SN-rGO the variation in cathodic current densities is more noticeable (approx.  $2.2 \text{ mA}\cdot\text{cm}^{-2}$  at  $j_L$ ). Furthermore, it seems that the insertion of heteroatoms in graphene structure favours the 4-electron pathway of the ORR giving lower current densities on the Pt ring. There are many works reporting the synergistic effect of N and S atoms as dopants in graphene materials for the ORR [3,5,50,51]. The introduction of N atoms into the graphene structure induces a charge density on the C carbon, leveraging the significant electronegativity difference between C and N. This charge separation facilitates the adsorption of  $\text{O}_2$  [52]. In contrast, although the electronegativity difference between S and C is less pronounced, and S is not traditionally considered an active site for the ORR, the dissimilarity in atomic radius (S: 110 pm, C: 70 pm) induces strain and introduces defects in graphene structures. These structural irregularities can potentially serve as sites for oxygen adsorption [11,26,27,52–54]. In our prior research [50], we observed the formation of a frustrated Lewis pair involving the lone electron pair of the nitrogen (N) atom and the energetically accessible d orbital of sulphur (S). This unique interaction strongly supports the dissociative mechanism of the ORR, actively inhibiting the formation of hydrogen peroxide ( $\text{H}_2\text{O}_2$ ) and favouring the more desirable 4-electron pathway.

MnZIF/SN-rGO is the material with the highest current densities and the more positive potential at  $-1 \text{ mA}\cdot\text{cm}^{-2}$  ( $E_{-1\text{mA}/\text{cm}^2}$ ) and half wave potential ( $E_{1/2}$ ). This means that it is the material with the best ORR performance of those studied as the closest to the thermodynamic value of the ORR (1.23 V vs. RHE) (see Table 3). It should be noted the error in  $E_{1/2}$  as the plateau is not complete defined for these materials. MnZIF/SN-rGO has the lowest overpotential for ORR, with an onset potential of 0.89 V, shifted to a more positive potential of around 120 mV compared to ZIF-TT and ZIF/rGO, and 80 mV compared to ZIF/SN-rGO. Besides, the MnZIF/SN-rGO develops outstanding catalytic behaviour towards ORR with a  $j_L$  almost equal to that of the Pt/C catalyst.

#### TbI2

The calculated number of electrons  $n$  was plotted as a function of the potential (Fig. 6a). ZIF-TT and ZIF/rGO present high  $n$  values, between 3.7 and 3.9 electrons, suggesting a mainly  $4 e^-$  pathway. However, the dual-doped materials show higher values closer to  $n = 4$  values, as well as a shift of the ORR to more positive potentials for ZIF/SN-rGO and MnZIF/SN-rGO.

For further study of the kinetic of the ORR, mass-transport corrected Tafel analysis was carried out (Fig. 6c). Two different linear regions can be distinguished in Tafel plots with different slopes. In the first one, at low overpotentials ( $E > 0.75 \text{ V}$ ), all the materials present Tafel slopes close to  $60 \text{ mV}\cdot\text{dec}^{-1}$  which is expected for the ORR in this potential region [55]. This value is attributed to the adsorption of oxygen species with a fast initial electron transfer followed by the rate-determining chemical step [56]; or to a first electron transfer becoming the rate determining step (rds) under Temkin adsorption conditions for the

oxygen reduction intermediates [57]. In the second region, at higher overpotentials ( $E < 0.75 \text{ V}$ ), all materials except for the MnZIF/SN-rGO, develop a Tafel slope of  $120 \text{ mV}\cdot\text{dec}^{-1}$  which can be interpreted through a mechanism involving the first electron transfer as rds and Langmuir adsorption conditions for the adsorbed intermediates [57,58].

In the case of MnZIF/SN-rGO, the Tafel slope at high overpotential is  $90 \text{ mV}\cdot\text{dec}^{-1}$  and differs to that of the other materials, and it would probably be the result of a competition of at least two electrochemical processes as rds: first, a chemical rate determining step after an electrochemical step, and second, the first electron transfer as rds [59].

Results could be explained due to the presence of different active sites associated with metallic centres from Co and Mn, and the active centres provided by graphene. At low overpotentials, the currents generated by the ORR are probably due to the reduction of  $\text{O}_2$  on the metallic active centres, while at higher overpotentials the presence of doped graphene could come into play. As seen in a previous work [27], doping of graphene with nitrogen and sulphur leads to a decrease in the overpotential for the ORR, which justifies the better performance of dual doped-based material compared to ZIF/rGO. Different works reported a Tafel slope value close to  $60 \text{ mV}\cdot\text{dec}^{-1}$  for carbonaceous materials at low overpotentials [60,61].

Different kinetic parameters were calculated according to the Tafel equation (Eq. (5)) at low and high overpotentials:

$$E = E^0 + \frac{2.303RT}{\alpha_c F} \log j_0 - \frac{2.303RT}{\alpha_c F} \log j \quad (5)$$

Where  $E$  is the recorded potential,  $E^0$  is the thermodynamic potential for the ORR (1.23 V vs RHE),  $R$  is the gas constant,  $T$  is the working temperature, and  $F$  is the Faraday constant. The obtained parameters are summarized in Table 2.

The exchange current density ( $j_0$ ), which is a key parameter for the evaluation of the catalytic activity, can be calculated from the y-intercept of the linear regions of the Tafel plot. As seen in Table 2, at low overpotentials MnZIF/SN-rGO presents a  $j_0$  one order of magnitude higher than that of ZIF/SN-rGO and ZIF/rGO, and 2 orders higher than ZIF-TT. Although it is not close to  $j_0$  of the Pt/C catalyst, it is comparable to other noble metal catalyst reported in the literature [62,63]. At high overpotential regions, all the materials present similar  $j_0$  values, about 3 orders of magnitude lower than Pt/C.

The cathodic transfer coefficient ( $\alpha_c$ ) is defined by Eq. (6) [64]:

$$\alpha_c = - \frac{RT}{F} \frac{d \ln |j_k|}{dE} \quad (6)$$

Notice that factor  $d \ln |j_k|/dE$  is the reciprocal of the Tafel slope. The calculated  $\alpha_c$  values shows a clear tendency, diminishing with the increase of the overpotential. Values at low overpotentials are close to the unity and decrease to 0.5 in the high overpotential region, describing a potential dependent mechanism of the ORR. High  $\alpha_c$  allows that low

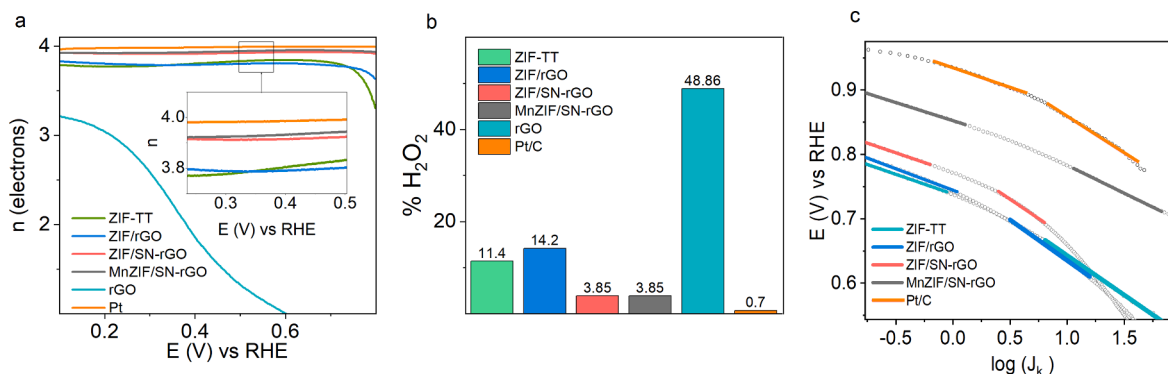


Fig. 6. A) number of electrons determined from rrde measurements vs  $e$  (v vs rhe); b) %  $\text{H}_2\text{O}_2$  produced during the ORR at 0.4 V for the ZIF-67 based materials and 0.2 V for rGO; and c) mass-transport corrected Tafel plot.

**Table 2**  
Different kinetic parameters obtained from Fig. 5 and Fig. 6.

Catalyst	E <sub>onset</sub> (V vs RHE)	E <sub>1</sub> mA/cm <sup>2</sup> (V vs RHE)	E <sub>1/2</sub> (V vs RHE)	Low η region			-	High η region		
				Tafel slope (mV dec <sup>-1</sup> )	α <sub>c</sub>	j <sub>0</sub> (mA cm <sup>-2</sup> )		Tafel slope (mV dec <sup>-1</sup> )	α <sub>c</sub>	j <sub>0</sub> (mA cm <sup>-2</sup> )
ZIF-TT	0.77	0.71	0.70	61	0.97	6.3·10 <sup>-9</sup>		119	0.49	1.1·10 <sup>-4</sup>
ZIF/rGO	0.77	0.73	0.69	63	0.93	2.4·10 <sup>-8</sup>		120	0.49	1·10 <sup>-4</sup>
ZIF/SN-rGO	0.81	0.76	0.71	61	0.97	3.29·10 <sup>-8</sup>		120	0.49	2.1·10 <sup>-4</sup>
MnZIF/SN-rGO	0.89	0.85	0.80	58	1	5.4·10 <sup>-7</sup>		90	0.55	1·10 <sup>-4</sup>
Pt/C	0.99	0.93	0.89	59	1	1.1·10 <sup>-5</sup>		118	0.50	1.3·10 <sup>-2</sup>

**Table 3**  
Heterogeneous rate constant determined at various applied potentials from K-L plot.

Material	k <sub>h</sub> (cm·s <sup>-1</sup> ) from K-L plot		
ZIF-TT	1.5·10 <sup>-2</sup>	3.7·10 <sup>-2</sup>	5.5·10 <sup>-3</sup>
ZIF/rGO	1.1·10 <sup>-3</sup>	2.7·10 <sup>-2</sup>	6.0·10 <sup>-3</sup>
ZIF/SN-rGO	1.7·10 <sup>-3</sup>	4.0·10 <sup>-3</sup>	8.2·10 <sup>-3</sup>
MnZIF/SN-rGO	2.5·10 <sup>-3</sup>	5.2·10 <sup>-2</sup>	7.6·10 <sup>-2</sup>

overpotential behaviour (where the reaction is governed by the kinetics) can persist to relatively high current densities unless a change on the mechanism or the coverage conditions of the electrode surface arises. As described above, at high overpotentials the first electron transfer is the rate determining step for the ORR.

3.3. Kinetic analysis 1. Koutecky-Levich method

For a mixed transport-kinetic controlled process, the reciprocal of the measured current density can be expressed as a sum of the reciprocals of the kinetic and limiting current densities (Koutecky-Levich equation (K-L))[65]:

$$\frac{1}{j} = \frac{1}{j_k} + \frac{1}{j_L} = \frac{1}{j_k} + \frac{1}{0.62nFD_{O_2}^{2/3}v^{-1/6}C_{O_2}\omega^{1/2}} \tag{7}$$

where j is the measured current density, j<sub>k</sub> and j<sub>L</sub> are the kinetic and the diffusion-limited current densities, respectively, n is the number of electrons transferred during the process, F is the Faraday constant (96485C/mol), C<sub>O<sub>2</sub></sub> is the saturation concentration of oxygen (1.13·10<sup>-6</sup> mol cm<sup>-3</sup>), D<sub>O<sub>2</sub></sub> is the diffusion coefficient of oxygen (2.22·10<sup>-5</sup> cm<sup>2</sup> s<sup>-1</sup>), v is the kinematic viscosity of the solution (1.1·10<sup>-2</sup> cm<sup>2</sup> s<sup>-1</sup>) and ω is the rotation speed of the electrode.

To study the kinetic of the reaction, LSVs were recorded at different rotation speeds (Figure S4). The diffusion-limiting current density of all the catalysts increases with the rotation speed due to the increase of the mass transport effect, thus, it is possible to apply the K-L plot analysis (1/j vs 1/ω<sup>1/2</sup>) (Fig. 7).

Linear trend is observed for the materials in Fig. 7. None of the catalysts show zero intercept implying additional mass transport limitations, which could be related to the presence of Nafion® on the surface of the material [66] also explaining the absence of a perfect plateau in the diffusion-controlled region. According to the K-L plots, the slope for each material changes with the selected potential. Since the theoretical

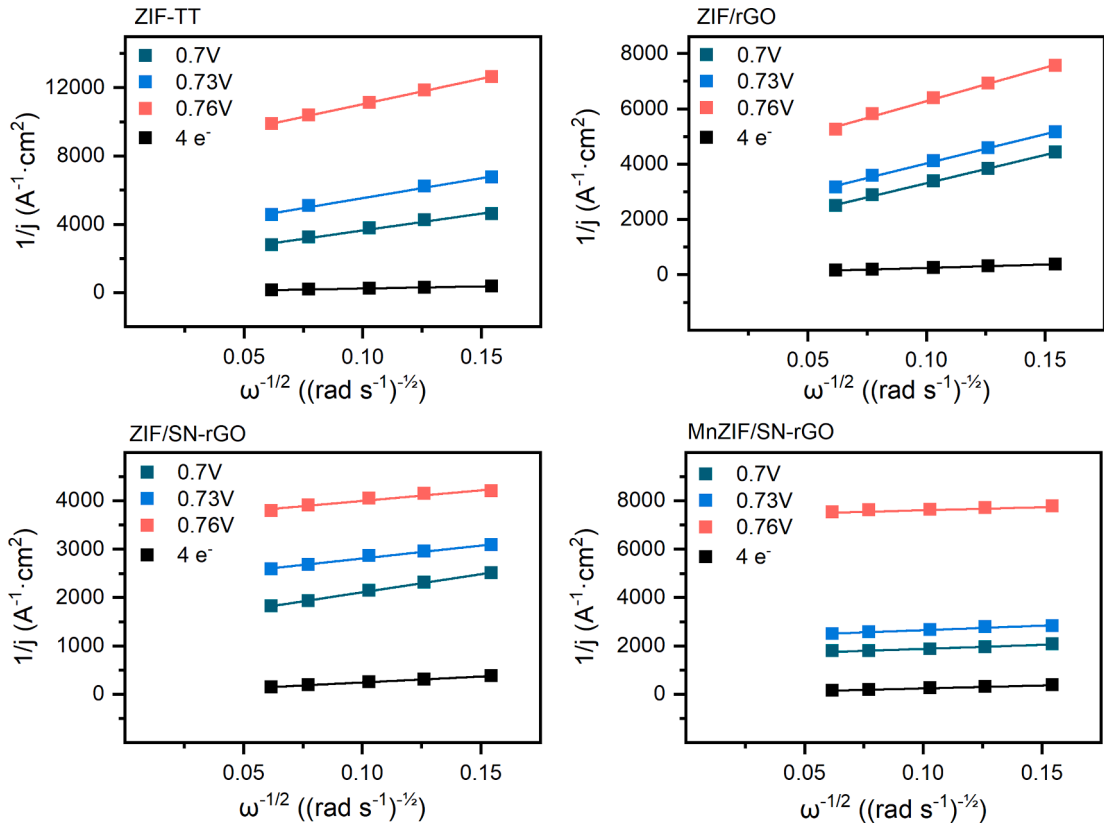


**Fig. 7.** Koutecky-Levich plots obtained at different potentials for the studied catalysts.

value from eq. (7) is independent of the potential, this changes should be ascribed to a change in the number of electrons transferred during the ORR, and thus, to a change in the mechanism with the potential, beside a change in the slope with the potential may imply non first order reaction [59]. The number of electrons transferred calculated from the K-L analysis is not quite accurate since it is an approximation for multi-steps reactions and flat surfaces, that it is not the condition in these studies. Thus, this work does not report the values [65,67]; however, a clear trend can be observed in which the inclination of the plot diminishes with increasing the overpotential, showing a behaviour closer to the theoretical curve calculated for oxygen reduction via 4 electrons. MnZIF/SN-rGO present the closest behaviour to the theoretical curve with a slope of  $2490 \text{ rad}^{1/2} \text{ s}^{-1/2} \text{ A}^{-1}$  at 0.8 V compared to  $2451 \text{ rad}^{1/2} \text{ s}^{-1/2} \text{ A}^{-1}$  for the theoretical  $4e^-$  curve. In the case ZIF-TT, ZIF/rGO and ZIF/SN-rGO the values are far from the theoretical curve (19706, 20,486 and  $4364 \text{ rad}^{1/2} \text{ s}^{-1/2} \text{ A}^{-1}$  respectively), therefore, a lower number of exchanged electrons is expected, being the ZIF/rGO the material with lower  $n$  value as can be seen in the  $n$  vs  $E$  graph (Fig. 6a).

As deduced from eq. (7), from the intercept of the K-L plot it is possible to determine the kinetic current density ( $j_k$ ), which is the current density given at a potential without mass-transport limitations and is directly related to the heterogeneous rate constant ( $k_h$ ):

$$\text{intercept} = \frac{1}{j_k} = \frac{1}{nFAk_hC_{O_2}} \quad (8)$$

The heterogeneous electron transfer rate constant was determined for the selected potentials for each material in Koutecky-Levich plots (Table 3). As explained above, it is not accurate to determine  $n$  from the K-L plot, thus, the  $n$  value used for calculating the rate constants are those obtained from eq. (3) (see Fig. 6). The results indicate that ZIF/rGO has faster electron transfer between the electrode and the oxygen molecule at the lower overpotential calculated for this material (0.71 V) compared to ZIF-67 at 0.76 V. This result can be justify considering the simultaneous reduction of higher amounts of  $H_2O_2$  (the reduction of this molecule is reported to have higher  $k_h$  than the oxygen reduction [68]). Nonetheless, at higher overpotentials where the ORR proceeds

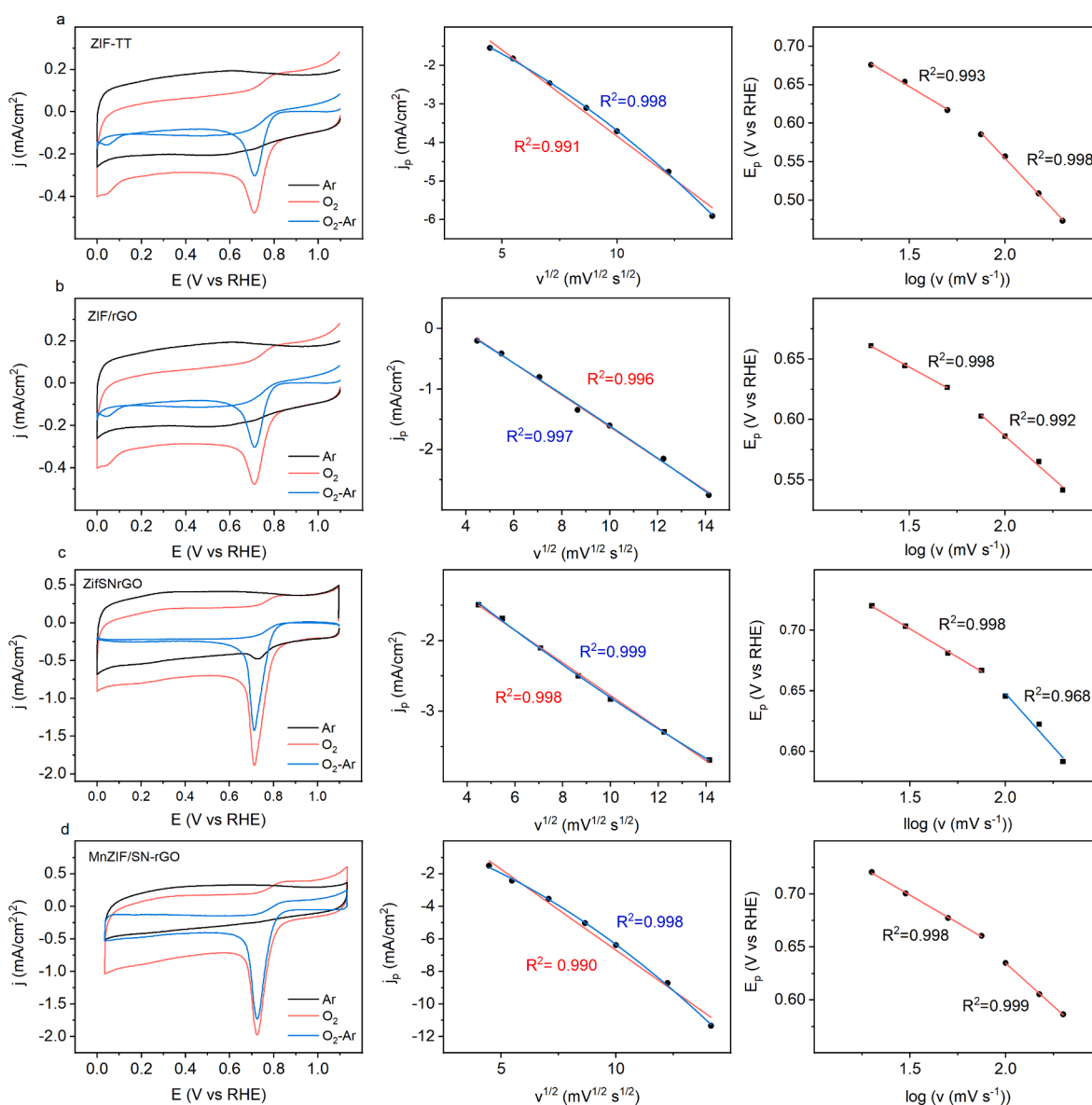


**Fig. 8.** Left: CVs recorded at  $10 \text{ mV s}^{-1}$  in  $O_2$  (red) and Ar (black) saturated electrolyte ( $0.5 \text{ M H}_2\text{SO}_4$ ), and their subtraction  $Ar-O_2$  (blue). Middle: peak current density of CV  $O_2$ -Ar as a function of the square root of scan rate (red lineal fit; blue quadratic fit). Right: peak potential of CV  $O_2$ -Ar as a function of the logarithm of the scan rate for (a) ZIF-TT, (b) ZIF/rGO, (c) ZIF/SN-rGO and (d) ZIF-Mn/SN-rGO. (For interpretation of the references to colour in this figure legend, the reader is referred to the web version of this article.)



mainly by  $4e^-$  pathway, it is the material with the lowest  $k_h$ . MnZIF/SN-rGO exhibits the highest  $k_h$  value followed by ZIF/SN-rGO and lastly by ZIF-TT.

Finally, it is also observed a decrease of  $k_h$  with the overpotential, that is explained according to the potentiodynamic theory defining  $k_h$  as follows [62]:

$$k_h = k^0 \exp \left[ \frac{-\alpha F \eta}{RT} \right] \quad (9)$$

### 3.4. Kinetic analysis 2. Study of the reduction of adsorbed $O_2$ (method 1)

For this analysis, cyclic voltammograms were recorded at different scan rates in 0.5 M  $H_2SO_4$  solution saturated with  $O_2$  or Ar. Fig. 8 left panels shows the voltammograms obtained at  $10 \text{ mV} \cdot \text{s}^{-1}$  together with those obtained subtracting the Ar-CV to the  $O_2$ -CV (denoted as  $O_2$ -Ar). The resulting CV minimizes the contribution of the capacitive and pseudocapacitive currents (double layer and functionalization red-ox processes, respectively), allowing to study both the reduction of oxygen adsorbed on the catalyst surface and the oxygen that diffuses from the bulk of the solution [69].

CVs in Fig. 8 are similar for all catalysts tested, developing a clear irreversible cathodic peak which is associated with the oxygen reduction. Although it is not appreciated a noticeable shift of the peak potential for the oxygen reduction at the materials studied ( $E_p \sim 0.7 \text{ V}$  vs RHE), there are differences in the currents, being the MnZIF/SN-rGO the catalyst that develops the highest current densities.

According to the theory of the potentiodynamic technique, for a diffusion-controlled process the peak current density ( $j_p$ ) varies linearly with the square root of the scan rate ( $v^{1/2}$ ) [67]:

$$j_p = 0.4463 n F A C_{O_2} \left( \frac{n F v D_{O_2}}{RT} \right)^{1/2} \quad (10)$$

On the other hand, when the reacting specie is strongly adsorbed on the surface of the electrode, in the absence of diffusion,  $j_p$  varies linearly with  $v$  [64,69]. Thus,  $j_p$  vs  $v^{1/2}$  plots given in Fig. 8 (middle panels) suggest that both, diffusion and surface adsorption, contribute to the ORR for ZIF-TT, ZIF/rGO, ZIF/SN-rGO and MnZIF/SN-rGO, since  $R^2$  for both processes seems to fit well with the experimental data obtained. Therefore, it is not possible to discriminate between the two processes as the rds. The catalytic materials without S and N have lower peak current densities, indicating that  $O_2$  adsorbs much stronger on ZIF/SN-rGO and MnZIF/SN-rGO.

Figure S5 shows the  $j_p$  vs  $v$  plots for all the catalyst. As expected, ZIF-TT and MnZIF/SN-rGO are the materials that fit better, which reveals the higher relevance of adsorption processes during the ORR. On the other hand, the lower  $R^2$  observed for ZIF/rGO and ZIF/SN-rGO confirms that these materials are mainly controlled by the oxygen diffusion.

For a totally irreversible process governed by diffusion the cathodic transfer coefficient ( $\alpha_c$ ) can be defined as [62,70]:

$$\alpha_c = - \frac{2.3RT}{2bF} \quad (11)$$

By using the slope  $b$  obtained from the plot of  $E_p$  vs  $\log v$  (Fig. 8 right panels). A good linear trend was found for the obtained  $E_p$  range (0.75 – 0.5 V) allowing the calculation of  $\alpha_c$ . In the case of ZIF-TT and MnZIF/SN-rGO, where the diffusion contribution is less important,  $\alpha_c$  can be calculated as follows [64,70]:

$$\alpha_c = - \frac{2.3RT}{bF} \quad (12)$$

As expected from Tafels analysis,  $\alpha_c$  depends on the potential, making it possible to distinguish different linear trends in  $E_p$  vs  $\log v$  plot and, in consequence, different  $\alpha_c$  values, concluding that the reaction mechanism changes intrinsically with the overpotential. Table 4 summarizes

**Table 4**

Different parameters obtained from  $E_p$  vs  $\log v$  plot in Fig. 8.

Catalyst	$E_p$ range (V vs RHE)	Slope (V/dec <sup>-1</sup> )	$\alpha_c$
ZIF-TT	0.70—0.60	0.148	0.40
	0.60—0.45	0.264	0.22
ZIF/rGO	0.70—0.65	0.086	0.44
	0.60—0.50	0.139	0.21
ZIF/SN-rGO	0.75—0.65	0.094	0.41
	0.65—0.55	0.018	0.17
MnZIF/SN-rGO	0.70—0.65	0.086	0.56
	0.60—0.45	0.139	0.36

the calculated  $\alpha_c$  using eq. (11) for ZIF/rGO and ZIF/SN-rGO and eq. (12) for ZIF-TT and MnZIF/SN-rGO. All the materials show a decrease of  $\alpha_c$  when increasing potential ( $E_p$ ). The  $\alpha_c$  obtained for the first linear region of  $E_p$  vs  $\log v$  variate between 0.40 and 0.56, however at more positive potential the obtained values are around 0.25, half of the previous one. Achieving the same trend as those previously obtained from Tafel plots. This make sense attending to the potential range where  $\alpha_c$  was calculated from Fig. 5. This decrease of  $\alpha_c$  may indicate a change in the reduction mechanism where the second electron transfer controls the overall rate and the first electron transfer becomes the determining step at higher overpotentials. These low  $\alpha_c$  values are usually associated with dissociative electron transfer processes, e.g., the dissociation of OOH intermediate during the second electron transfer [71].

The most accepted ORR mechanism in acidic media for M–N based catalysts comprises the decomposition of OOH intermediate [52]:



Where  $*$  is an electroactive site in the surface of the catalyst.

The first electron transfer (eq. (14)) is not expected to involve any bond-breaking process, resulting in a symmetric activation energy and  $\alpha_c = 0.5$ . Furthermore, the relatively low  $H_2O_2$  production observed for all catalysts in Fig. 6b indicates that the O–O bond breaking occurs prior to the third electron transfer step, inhibiting the production of  $H_2O_2$ . Consequently, the O–O bond breaking is probably associated with the second electron transfer (eq. (15)). Since the O–O bond is considered to be strong, the second electron transfer should be the rds for the studied potential range (0.60 – 0.45 E vs RHE) [70–72]. However, a potential dependence of  $\alpha_c$  is observed, and consequently, it must be reflected in the mechanism of O–O bond breaking.

Results presented in this and the previous sections, show a decrease of  $\alpha_c$  with the potential from 1 to approximately 0.5 indicating that when the overpotential is very small, the first and second electron transfers are independent processes, giving a sequential mechanism, where the second electron transfer is accompanied by the O–O bond breaking. A gradually change from this sequential mechanism to a mechanism where the electron transfer and the bond-splitting occurs simultaneously, may result in an  $\alpha_c$  significantly lower than 0.5 [73]. Nevertheless, if this mechanism is only applied for the second electron transfer, then the charge transfer coefficient should never drop below one if the first electron was transferred as an independent step. Then, it is suggested that the change in the mechanism goes from the mentioned mechanism, where two electrons are transferred sequentially followed by the bond splitting to a mechanism where the electron transfer and the bond dissociation occurs simultaneously [52,73,74].

### 3.5. Kinetic analysis 3. Study of the reduction of adsorbed O<sub>2</sub> (method 2)

This second method for the study of the reduction of the adsorbed O<sub>2</sub> on the catalyst consists in recording two consecutive CVs in O<sub>2</sub> saturated medium and subtract the second scan from the first one, obtaining a differential CV (CV<sub>1-2</sub>). This allows to minimize the contribution of the diffusion of oxygen as much as possible to the peak current density. In this method the reduction peak can be associated almost totally to the reduction of the adsorbed O<sub>2</sub>. The CV<sub>1-2</sub> was obtained at different scan rates. These CVs show almost symmetrical peaks for all the materials, with  $j_p$  values between  $-1$  and  $-10.5 \text{ mA cm}^{-2}$ , ZIF-TT and MnZIF/SN-rGO develop higher current densities (Fig. 9) indicating that the contribution of the adsorbed O<sub>2</sub> is much more significant than in ZIF/rGO and ZIF/SN-rGO which agrees with weak diffusion behaviour described in the previous section.

As seen in Fig. 9 left panel, the developed peaks are much more symmetrical at low scan rates than at higher scan rates, where the part of the peak located at less positive potentials becomes larger when increasing the scan rate. The effect is not due to an unaccounted

contribution of O<sub>2</sub> diffusion, as it decreases with the scan rate. Thus, this effect can be probably ascribed to the changes in the kinetics of the reduction of the adsorbed O<sub>2</sub>. This phenomenon is more notable in ZIF-TT and ZIF/SN-rGO, as expected from previous analysis.

The obtained currents in the CV<sub>1-2</sub> are consistent with the weak diffusion behaviour of ZIF-TT and MnZIF/SN-rGO, developing higher current densities because of the more significant contribution of adsorbed oxygen. From the full width at half-maximum ( $\Delta E_{1/2}$ ) plotted vs  $v^{1/2}$  of the CV<sub>1-2</sub> peaks, it is possible to determine  $\alpha_c$  (Fig. 9 middle panel). According to Laviron's method [75], for a diffusionless process  $\alpha_c$  can be calculated as follows:

$$\alpha_c = \frac{62.5 \text{ mV}}{\Delta E_{1/2}} \quad (18)$$

Once  $\alpha_c$  is calculated, it was plotted vs  $E_p$  revealing an almost linear trend (Fig. 9 right panel). The obtained plots show a decrease of  $\alpha_c$  with the peak potential, and consequent, with the scan rate, indicating a potential dependent mechanism of the ORR in these materials. At low scan rates high  $E_p$  is obtained and  $\alpha_c$  is close to the unity, similar to the

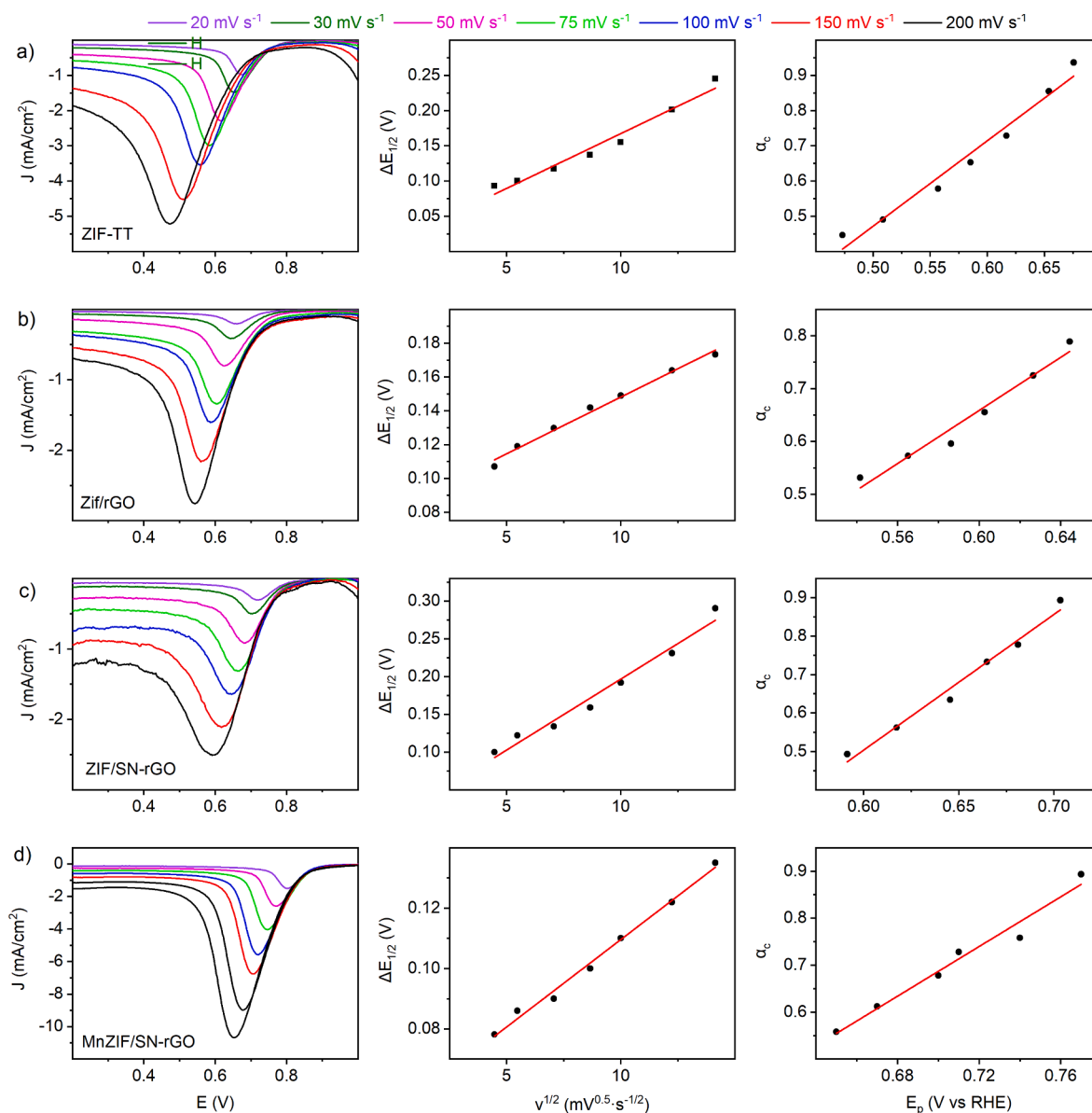


**Fig. 9.** Left: CV<sub>1-2</sub> at different scan rates recorded in O<sub>2</sub> saturated 0.5 M H<sub>2</sub>SO<sub>4</sub> medium. Middle: full width at half-maximum of the peaks of the differential voltammograms ( $\Delta E_{1/2}$ ) vs  $v$ . Right:  $\alpha_c$  vs  $E_p$  for a) ZIF-TT, b) ZIF/rGO, c) ZIF/SN-rGO and d) MnZIF/SN-rGO.

results obtained from Tafel analysis experiments at low overpotentials. At higher scan rates (lower  $E_p$  is obtained)  $\alpha_c$  values approx. to 0.5 closer to those obtained at high overpotentials in [section 3.2](#).

For all investigated materials, a noteworthy trend emerges: at more positive potentials, the calculated charge transfer coefficients approach unity, signifying a nearly complete electron transfer process. As potentials decrease, these coefficients gradually diminish, reaching values between 0.5 and 0.6 at lower potentials. This nuanced interplay between potential and electron transfer kinetics illuminates the intricate mechanisms governing the oxygen reduction reaction on these graphene materials.

In the case of ZIF-TT, the  $\alpha_c$  values range from 0.53 to 0.8 within the studied potential window (0.54 – 0.65 V vs RHE). For MnZIF/SN-rGO, within the potential range of 0.75 to 0.65 V,  $\alpha_c$  varies from 0.9 to 0.55 (refer to [Fig. 9](#)).

Conversely, the calculated  $\alpha_c$  values for ZIF/rGO and ZIF/SN-rGO range from 1.03 to 0.53 and 1.05 to 0.49, respectively, in the potential range between 0.55 and 0.75 V. A notable disparity with the summarized values in [Table 4](#) is evident. This discrepancy could be attributed to the contribution of O<sub>2</sub> diffusion in the studies presented in [section 3.2](#), as it was not removed from the voltammogram, resulting in lower  $\alpha_c$  values. As previously noted, for these materials, the ORR is primarily controlled by the diffusion of O<sub>2</sub>.

The calculated charge transfer coefficients at different potentials consistently align with the results from earlier sections (refer to [Table 2](#) and [Table 4](#)). This agreement underscores the robustness of our findings, emphasizing the convergence of outcomes from diverse analytical methods. These concurrent assessments validate the reliability and accuracy of the charge transfer coefficients reported in this study.

Special attention is warranted for observed variations in charge transfer coefficients at lower overpotentials. These results diverge from those obtained for similar potentials in the previous section, potentially due to the unaccounted influence of diffusive oxygen contribution. This underscores the importance of meticulous consideration and appropriate adjustments for various factors impacting the kinetic analysis of the oxygen reduction reaction, emphasizing the complexity inherent in elucidating the underlying mechanisms in such electrochemical systems.

#### 4. Conclusions

In this study, graphene oxide (GO) served as a successful precursor for synthesizing ZIF-67 supported on reduced graphene oxide (rGO). The in-situ growth of ZIF-67 crystals directly on the GO surface was followed by a thermal treatment step, resulting in the final catalyst (ZIF/rGO). Introduction of thiourea during the thermal treatment yielded a second catalyst based on ZIF-67 supported on N and S dual-doped rGO. Furthermore, incorporating a Mn precursor during ZIF-67 crystal growth onto graphene produced a Mn-modified ZIF-67 supported on SN-rGO. Those materials were characterized and compared with ZIF-67 raw thermal treated material. The use of graphene produces a more homogeneous dispersion and less agglomeration of the ZIF-67 after heat treatment. The addition of rGO to ZIF-67 results in an increase of the cathodic currents related to ORR, however, the production of H<sub>2</sub>O<sub>2</sub> also increased.

On the other hand, the insertion of N and S shows an increase of the electrocatalytic activity by reducing the overpotential and the H<sub>2</sub>O<sub>2</sub> production and increasing the currents densities. Mn-modified material was found to be the most performing catalyst, resulting in a decrease of the overpotential of up to 140 mV at  $-1 \text{ mA}\cdot\text{cm}^{-2}$  and an exchange current density two orders of magnitude higher than that of ZIF-TT at low overpotentials. XPS analysis revealed that Mn favours the insertion of oxygen and the formation of Co<sub>3</sub>O<sub>4</sub> which is reported to have high electrocatalytic activity towards ORR. Tafel analysis exposed a potential dependent mechanism for the ORR on these materials. MnZIF/SN-rGO shows different behaviour at high overpotential with a Tafel slope of  $90 \text{ mV}\cdot\text{dec}^{-1}$ , suggesting a competition between two rate determining

steps, the first electron transfer and a chemical step following an electrochemical step which was supported by the charge transfer analysis studies by different methods.

#### CRediT authorship contribution statement

**S. Fajardo:** Writing – original draft, Visualization, Methodology, Investigation. **P. Ocón:** Writing – review & editing, Visualization, Supervision, Resources, Project administration, Funding acquisition, Conceptualization, Visualization, Writing – review & editing, Supervision, Resources, Project administration, Funding acquisition. **A. Arranz:** Writing – review & editing, Validation, Methodology, Investigation, Formal analysis. **J.L. Rodríguez:** Writing – review & editing, Visualization, Methodology, Investigation, Formal analysis. **E. Pastor:** Writing – review & editing, Visualization, Supervision, Resources, Project administration, Funding acquisition, Conceptualization, Visualization, Writing – review & editing, Supervision, Resources, Project administration, Funding acquisition.

#### Declaration of competing interest

The authors declare that they have no known competing financial interests or personal relationships that could have appeared to influence the work reported in this paper.

#### Data availability

Data will be made available on request.

#### Acknowledgements

This work has been supported by the Ministerio de Ciencia e Innovación (MCIN) under projects PCI2020-112249, PID2020-116712RB-C21 and PID2020-117586RB-I00 funded by MCIN/AEI/10.13039/501100011033. S. Fajardo acknowledges the MCIN for the pre-doctoral grant (PRE2018-085718). The author thanks SEGAI for its collaboration during the physical characterization of the studied materials.

**Authors Contributions:** Investigation, methodology, visualization, writing-original draft, S.F.; investigation, methodology, validation, formal analysis, writing-review & editing, A.A. and J.L.R.; conceptualization, visualization, writing-review & editing, supervision, resources, project administration, funding acquisition, P.O. and E.P.

#### Appendix A. Supplementary data

Supplementary data to this article can be found online at <https://doi.org/10.1016/j.jcat.2024.115448>.

#### References

- [1] M. Kuang, Q. Wang, P. Han, G. Zheng, Cu, co-embedded N-enriched mesoporous Carbon for efficient oxygen reduction and hydrogen evolution reactions, *Adv. Energy Mater.* 7 (2017), <https://doi.org/10.1002/aenm.201700193>.
- [2] R. Zhang, M. Tahir, S. Ding, M.A. Qadeer, H. Li, Q.X. Zeng, R. Gao, L. Wang, X. Zhang, L. Pan, J.J. Zou, Promotion of nitrogen reserve and electronic regulation in bamboo-like Carbon tubules by cobalt Nanoparticles for highly efficient ORR, *ACS Appl. Energy Mater.* 3 (2020) 2323–2330, <https://doi.org/10.1021/acsaem.9b01617>.
- [3] D.M. Fernandes, P. Mathumba, A.J.S. Fernandes, E.I. Iwuoha, C. Freire, Towards efficient oxygen reduction reaction electrocatalysts through graphene doping, *Electrochim. Acta.* 319 (2019) 72–81, <https://doi.org/10.1016/j.electacta.2019.06.175>.
- [4] L. Osmieri, L. Pezzolato, S. Specchia, Recent trends on the application of PGM-free catalysts at the cathode of anion exchange membrane fuel cells, *Curr. Opin. Electrochem.* 9 (2018) 240–256, <https://doi.org/10.1016/j.coelec.2018.05.011>.
- [5] Y. Chen, Z. Shi, S. Li, J. Feng, B. Pang, L. Yu, W. Zhang, L. Dong, N, S-codoped graphene supports for ag-MnFe<sub>2</sub>O<sub>4</sub> nanoparticles with improved performance for oxygen reduction and oxygen evolution reactions, *J. Electroanal. Chem.* 860 (2020) 113930, <https://doi.org/10.1016/j.jelechem.2020.113930>.

- [6] M.A. Molina-García, N.V. Rees, "Metal-free" electrocatalysis: Quaternary-doped graphene and the alkaline oxygen reduction reaction, *Appl. Catal. A Gen.* 553 (2018) 107–116, <https://doi.org/10.1016/j.apcata.2017.12.014>.
- [7] Y. Tan, Z. Zhang, Z. Lei, W. Wu, W. Zhu, N. Cheng, S. Mu, Thiourea-zeolitic imidazolate Framework-67 assembly derived Co–CoO nanoparticles encapsulated in N, S doped open carbon shell as bifunctional oxygen electrocatalyst for rechargeable flexible solid Zn–Air batteries, *J. Power Sources.* 473 (2020) 228570, <https://doi.org/10.1016/j.jpowsour.2020.228570>.
- [8] A. Al Nafey, A. Addad, B. Sieber, G. Chastanet, A. Barras, S. Szunerits, R. Boukherroub, Reduced graphene oxide decorated with Co<sub>3</sub>O<sub>4</sub> nanoparticles (rGO-Co<sub>3</sub>O<sub>4</sub>) nanocomposite: a reusable catalyst for highly efficient reduction of 4-nitrophenol, and Cr (VI) and dye removal from aqueous solutions, *Chem. Eng. J.* 322 (2017) 375–384, <https://doi.org/10.1016/j.cej.2017.04.039>.
- [9] Y.T. Zhang, S.Y. Li, N.N. Zhang, G. Lin, R.Q. Wang, M.N. Yang, K.K. Li, A carbon catalyst doped with Co and N derived from the metal-organic framework hybrid (ZIF-8@ZIF-67) for efficient oxygen reduction reaction, *Xinxing Tan Cailiao/new Carbon Mater.* 38 (2023) 200–210, [https://doi.org/10.1016/S1872-5805\(22\)60609-7](https://doi.org/10.1016/S1872-5805(22)60609-7).
- [10] T. Varga, G. Ballai, L. Vászrhelyi, H. Hapel, Á. Kukovecz, Z. Kónya, Co<sub>4</sub>N/ nitrogen-doped graphene: a non-noble metal oxygen reduction electrocatalyst for alkaline fuel cells, *Appl. Catal. B Environ.* 237 (2018) 826–834, <https://doi.org/10.1016/j.apcatb.2018.06.054>.
- [11] S. Fajardo, P. Ocón, J.L. Rodríguez, E. Pastor, Co supported on N and S dual-doped reduced graphene oxide as highly active oxygen-reduction catalyst for direct ethanol fuel cells, *Chem. Eng. J.* 461 (2023), <https://doi.org/10.1016/j.cej.2023.142053>.
- [12] Y. Zhao, K. Watanabe, K. Hashimoto, Self-supporting oxygen reduction electrocatalysts made from a nitrogen-rich network polymer, *J. Am. Chem. Soc.* 134 (2012) 19528–19531, <https://doi.org/10.1021/ja3085934>.
- [13] C. Duan, Y. Yu, H. Hu, Recent progress on synthesis of ZIF-67-based materials and their application to heterogeneous catalysis, *green, Energy Environ.* 7 (2022) 3–15, <https://doi.org/10.1016/j.jee.2020.12.023>.
- [14] A. Phan, C.J. Doonan, F.J. Uribe-Romo, C.B. Knobler, M.O. Keeffe, O.M. Yaghi, Capture properties of zeolitic imidazolate frameworks, *Acc. Chem. Res.* 43 (2010) 58–67, <https://doi.org/10.1021/ar900116g>.
- [15] J. Qin, S. Wang, X. Wang, Visible-light reduction CO<sub>2</sub> with dodecahedral zeolitic imidazolate framework ZIF-67 as an efficient co-catalyst, *Appl. Catal. B Environ.* 209 (2017) 476–482, <https://doi.org/10.1016/j.apcatb.2017.03.018>.
- [16] V. Shrivastav, S. Sundriyal, A. Kaur, U.K. Tiwari, S. Mishra, A. Deep, Conductive and porous ZIF-67/PEDOT hybrid composite as superior electrode for all-solid-state symmetrical supercapacitors, *J. Alloys Compd.* 843 (2020) 155992, <https://doi.org/10.1016/j.jallcom.2020.155992>.
- [17] Y. Gorlin, T.F. Jaramillo, A bifunctional nonprecious metal catalyst for oxygen reduction and water oxidation, *J. Am. Chem. Soc.* 132 (2010) 13612–13614, <https://doi.org/10.1021/ja104587v>.
- [18] S.S. Selvasundarasekar, T.K. Bijoy, S. Kumaravel, A. Karmakar, R. Madhu, K. Bera, S. Nagappan, H.N. Dhandapani, G.A.M. Mersal, M.M. Ibrahim, D. Sarkar, S. M. Yusuf, S.C. Lee, S. Kundu, Effective formation of a mn-ZIF-67 nanofibrous network via electrospinning: an active electrocatalyst for OER in alkaline medium, *ACS Appl. Mater. Interfaces.* 14 (2022) 46581–46594, <https://doi.org/10.1021/acsami.2c12643>.
- [19] Y. Liang, H. Wang, J. Zhou, Y. Li, J. Wang, T. Regier, H. Dai, Covalent hybrid of spinel manganese-cobalt oxide and graphene as advanced oxygen reduction electrocatalysts, *J. Am. Chem. Soc.* 134 (2012) 3517–3523, <https://doi.org/10.1021/ja210924t>.
- [20] Y.V. Kaneti, Y. Guo, N.L.W. Septiani, M. Iqbal, X. Jiang, T. Takei, B. Yuliarto, Z. A. Althman, D. Golberg, Y. Yamauchi, Self-templated fabrication of hierarchical hollow manganese-cobalt phosphide yolk-shell spheres for enhanced oxygen evolution reaction, *Chem. Eng. J.* 405 (2021) 126580, <https://doi.org/10.1016/j.cej.2020.126580>.
- [21] C. Fan, X. Wu, M. Li, X. Wang, Y. Zhu, G. Fu, T. Ma, Y. Tang, Surface chemical reconstruction of hierarchical hollow inverse-spinel manganese cobalt oxide boosting oxygen evolution reaction, *Chem. Eng. J.* 431 (2022) 133829, <https://doi.org/10.1016/j.cej.2021.133829>.
- [22] P.W. Menezes, A. Indra, N.R. Sahraie, A. Bergmann, P. Strasser, M. Driess, Cobalt-manganese-based spinels as multifunctional materials that unify catalytic water oxidation and oxygen reduction reactions, *ChemSusChem.* 8 (2015) 164–167, <https://doi.org/10.1002/cssc.201402699>.
- [23] K. Kakaei, M.D. Esrafi, A. Ehsani, Oxygen Reduction Reaction (2019), <https://doi.org/10.1016/B978-0-12-814523-4.00006-X>.
- [24] I.C. Man, I. Trancà, S.G. Soriga, First principle studies of oxygen reduction reaction on N doped graphene: impact of N concentration, position and co-adsorbate effect, *Appl. Surf. Sci.* 510 (2020), <https://doi.org/10.1016/j.apsusc.2020.145470>.
- [25] T. Zhang, C. He, F. Sun, Y. Ding, M. Wang, L. Peng, J. Wang, Y. Lin, Co<sub>3</sub>O<sub>4</sub> nanoparticles anchored on nitrogen-doped reduced graphene oxide as a multifunctional catalyst for H<sub>2</sub>O<sub>2</sub> reduction, oxygen reduction and evolution reaction, *Sci. Rep.* 7 (2017) 43638, <https://doi.org/10.1038/srep43638>.
- [26] J. Xu, G. Dong, C. Jin, M. Huang, L. Guan, Sulfur and nitrogen co-doped, few-layered graphene oxide as a highly efficient electrocatalyst for the oxygen-reduction reaction, *ChemSusChem.* 6 (2013) 493–499, <https://doi.org/10.1002/cssc.201200564>.
- [27] L.M. Rivera, S. Fajardo, C. Arévalo, G. García, E. Pastor, S- and N-doped graphene nanomaterials for the oxygen reduction reaction, *Catalysts.* 7 (2017) 278, <https://doi.org/10.3390/catal7090278>.
- [28] N. Iwashita, C.R. Park, H. Fujimoto, M. Shiraishi, M. Inagaki, Specification for a standard procedure of X-ray diffraction measurements on carbon materials, *Carbon* n. y. 42 (2004) 2131, <https://doi.org/10.1016/j.carbon.2004.05.027>.
- [29] M. Kuang, Q. Wang, P. Han, G. Zheng, Cu, co-embedded N-enriched mesoporous Carbon for efficient oxygen reduction and hydrogen evolution reactions, *Adv. Energy Mater.* 7 (2017) 1–8, <https://doi.org/10.1002/aenm.201700193>.
- [30] C. Botas, P. Álvarez, C. Blanco, R. Santamaría, M. Granda, P. Ares, F. Rodríguez-Reinos, R. Menéndez, The effect of the parent graphite on the structure of graphene oxide, *Carbon* n. y. 50 (2012) 275–282, <https://doi.org/10.1016/j.carbon.2011.08.045>.
- [31] G. Lemes, D. Sebastián, E. Pastor, M.J. Lázaro, N-doped graphene catalysts with high nitrogen concentration for the oxygen reduction reaction, *J. Power Sources.* 438 (2019), <https://doi.org/10.1016/j.jpowsour.2019.227036>.
- [32] V. Sannasi, K. Subbian, Influence of Moringa oleifera gum on two polymorphs synthesis of MnO<sub>2</sub> and evaluation of the pseudo-capacitance activity, *J. Mater. Sci. Mater. Electron.* 31 (2020) 17120–17132, <https://doi.org/10.1007/s10854-020-04272-z>.
- [33] S. Zhang, Q. Yang, Z. Li, W. Wang, C. Wang, Z. Wang, Zeolitic imidazole framework templated synthesis of nanoporous carbon as a novel fiber coating for solid-phase microextraction, *Analyst.* 141 (2016) 1127–1135, <https://doi.org/10.1039/c5an02059j>.
- [34] C. Nunes, A. Mahendrasingam, R. Suryanarayanan, Quantification of crystallinity in substantially amorphous materials by synchrotron X-ray powder diffractometry, *Pharm. Res.* 22 (2005) 1942–1953, <https://doi.org/10.1007/s11095-005-7626-9>.
- [35] Y. Yan, F.Z. Nashath, S. Chen, S. Manickam, S.S. Lim, H. Zhao, E. Lester, T. Wu, C. H. Pang, Synthesis of graphene: potential carbon precursors and approaches, *Nanotechnol. Rev.* 9 (2020) 1284–1314, <https://doi.org/10.1515/ntrev-2020-0100>.
- [36] R. Hesse, M. Weiß, R. Szargan, P. Streubel, R. Denecke, Comparative study of the modelling of the spectral background of photoelectron spectra with the Shirley and improved Tougaard methods, *J. Electron Spectrosc. Relat. Phenomena.* 186 (2013) 44–53, <https://doi.org/10.1016/j.elspec.2013.01.020>.
- [37] D. Barreca, C. Massignat, S. Daolio, M. Fabrizio, C. Piccirillo, L. Armelao, E. Tondello, Composition and microstructure of cobalt oxide thin films obtained from a novel cobalt (II) precursor by chemical vapor deposition, *Chem. Mater.* 13 (2001) 588–593, <https://doi.org/10.1021/cm001041x>.
- [38] D.G. Castner, P.R. Watson, I.Y. Chan, X-ray absorption spectroscopy, X-ray photoelectron spectroscopy, and analytical electron microscopy studies of cobalt catalysts. 1. Characterization of calcined catalysts, *J. Phys. Chem.* 93 (1989) 3188–3194, <https://doi.org/10.1021/j100345a061>.
- [39] S. Bibi, E. Pervaiz, M. Yang, O. Rabi, Mof embedded and Cu doped ceo2 nanostructures as efficient catalyst for adipic acid production: green catalysis, *Catalysts.* 11 (2021) 1–19, <https://doi.org/10.3390/catal11030304>.
- [40] L. Xing, J. Liu, T. Qi, L. Wang, Z. Wang, S. Zhang, Superior energy-saving catalyst of Mn@ZIF67 for reclaiming byproduct in wet magnesia desulfurization, *Appl. Catal. B Environ.* 275 (2020) 119143, <https://doi.org/10.1016/j.apcatb.2020.119143>.
- [41] W. Song, Z. Ren, S.Y. Chen, Y. Meng, S. Biswas, P. Nandi, H.A. Elsen, P.X. Gao, S. L. Suib, Ni- and mn-promoted mesoporous Co<sub>3</sub>O<sub>4</sub>: a stable bifunctional catalyst with Surface-structure-dependent activity for oxygen reduction reaction and oxygen evolution reaction, *ACS Appl. Mater. Interfaces.* 8 (2016) 20802–20813, <https://doi.org/10.1021/acsami.6b06103>.
- [42] J. Xu, P. Gao, T.S. Zhao, Non-precious Co<sub>3</sub>O<sub>4</sub> nano-rod electrocatalyst for oxygen reduction reaction in anion-exchange membrane fuel cells, *Energy Environ. Sci.* 5 (2012) 5333–5339, <https://doi.org/10.1039/c1ee01431e>.
- [43] X. Feng, D.F. Cox, Oxidation of MnO(100) and NaMnO<sub>2</sub> formation: Characterization of Mn<sup>2+</sup> and Mn<sup>3+</sup> surfaces via XPS and water TPD, *Surf. Sci.* 675 (2018) 47–53, <https://doi.org/10.1016/j.susc.2018.04.022>.
- [44] M. Risch, K.A. Stoerzinger, B. Han, T.Z. Regier, D. Peak, S.Y. Sayed, C. Wei, Z. Xu, Y. Shao-Horn, Redox processes of manganese oxide in catalyzing oxygen evolution and reduction: an in situ soft X-ray absorption spectroscopy study, *J. Phys. Chem. c.* 121 (2017) 17682–17692, <https://doi.org/10.1021/acs.jpcc.7b05592>.
- [45] R.B. Valim, M.C. Santos, M.R.V. Lanza, S.A.S. MacHado, F.H.B. Lima, M. L. Calegari, Oxygen reduction reaction catalyzed by ε-MnO<sub>2</sub>: influence of the crystalline structure on the reaction mechanism, *Electrochim. Acta.* 85 (2012) 423–431, <https://doi.org/10.1016/j.electacta.2012.08.075>.
- [46] I. Roche, E. Chaînet, M. Chatenet, J. Vondrák, Carbon-supported manganese oxide nanoparticles as electrocatalysts for the oxygen reduction reaction (ORR) in alkaline medium: physical characterizations and ORR mechanism, *J. Phys. Chem. c.* 111 (2007) 1434–1443, <https://doi.org/10.1021/jp0647986>.
- [47] J. Baltrusaitis, P.M. Jayaweera, V.H. Grassian, XPS study of nitrogen dioxide adsorption on metal oxide particle surfaces under different environmental conditions, *Phys. Chem. Chem. Phys.* 11 (2009) 8295–8305, <https://doi.org/10.1039/b907584d>.
- [48] M.J. Webb, P. Palmgren, P. Pal, O. Karis, H. Grennberg, A simple method to produce almost perfect graphene on highly oriented pyrolytic graphite, *Carbon* n. y. 49 (2011) 3242–3249, <https://doi.org/10.1016/j.carbon.2011.03.050>.
- [49] J. Wu, W. Wang, Z. Wang, Porphin-based carbon dots for "turn off-on" phosphate sensing and cell imaging, *Nanomaterials.* 10 (2020) 1–16, <https://doi.org/10.3390/nano10020326>.
- [50] F. Aguilar-Galindo, S. Fajardo-Rodríguez, J.M.L. Poyato, E. Pastor, J.R. Avilés-Moreno, P. Ocón, Outstanding inhibition of H<sub>2</sub>O<sub>2</sub> generation in doubly doped graphene: the synergy of two heteroatoms opens a new chemical path, *Carbon* n. y. 216 (2024), <https://doi.org/10.1016/j.carbon.2023.118499>.



- [51] N. Daems, X. Sheng, I.F.J. Vankelecom, P.P. Pescarmona, Metal-free doped carbon materials as electrocatalysts for the oxygen reduction reaction, *J. Mater. Chem. a* 2 (2014) 4085–4110, <https://doi.org/10.1039/c3ta14043a>.
- [52] L. lai Liu, M. xuan Ma, H. Xu, X. ying Yang, X. yu Lu, P. Yang, H. Wang, S-doped M-N-C catalysts for the oxygen reduction reaction: synthetic strategies, characterization, and mechanism, *J. Electroanal. Chem.* 920 (2022) 116637, <https://doi.org/10.1016/j.jelechem.2022.116637>.
- [53] J. Lee, S. Noh, N.D. Pham, J.H. Shim, Top-down synthesis of S-doped graphene nanosheets by electrochemical exfoliation of graphite: metal-free bifunctional catalysts for oxygen reduction and evolution reactions, *Electrochim. Acta.* 313 (2019) 1–9, <https://doi.org/10.1016/j.electacta.2019.05.015>.
- [54] Z. Wang, P. Li, Y. Chen, J. He, W. Zhang, O.G. Schmidt, Y. Li, Pure thiophene-sulfur doped reduced graphene oxide: synthesis, structure, and electrical properties, *Nanoscale.* 6 (2014) 7281–7287, <https://doi.org/10.1039/c3nr05061k>.
- [55] T. Shinagawa, A.T. Garcia-Esparza, K. Takanabe, Insight on tafel slopes from a microkinetic analysis of aqueous electrocatalysis for energy conversion, *Sci. Rep.* 5 (2015) 1–21, <https://doi.org/10.1038/srep13801>.
- [56] A. Damjanovic, V. Brusic, Electrode kinetics of oxygen reduction on oxide-free platinum electrodes, *Electrochim. Acta.* 12 (1967) 615–628, [https://doi.org/10.1016/0013-4686\(67\)85030-8](https://doi.org/10.1016/0013-4686(67)85030-8).
- [57] C.F. Zinola, A.M. Castro Luna, W.E. Triaca, A.J. Arvia, Electroreduction of molecular oxygen on preferentially oriented platinum electrodes in acid solution, *J. Appl. Electrochem.* 24 (1994) 119–125, <https://doi.org/10.1007/BF00247782>.
- [58] N.M. Marković, R.R. Adžić, B.D. Cahan, E.B. Yeager, Structural effects in electrocatalysis: oxygen reduction on platinum low index single-crystal surfaces in perchloric acid solutions, *J. Electroanal. Chem.* 377 (1994) 249–259, [https://doi.org/10.1016/0022-0728\(94\)03467-2](https://doi.org/10.1016/0022-0728(94)03467-2).
- [59] G. Pérez, E. Pastor, C.F. Zinola, A novel Pt/Cr/Ru/C cathode catalyst for direct methanol fuel cells (DMFC) with simultaneous methanol tolerance and oxygen promotion, *Int. J. Hydrogen Energy.* 34 (2009) 9523–9530, <https://doi.org/10.1016/j.ijhydene.2009.09.088>.
- [60] C. Li, Z. Chen, A. Kong, Y. Ni, F. Kong, Y. Shan, High-rate oxygen electroreduction over metal-free graphene foams embedding P-N coupled moieties in acidic media, *J. Mater. Chem. a* 6 (2018) 4145–4151, <https://doi.org/10.1039/c7ta08186c>.
- [61] S.K. Singh, K. Takeyasu, K. Homma, S. Ito, T. Morinaga, Y. Endo, M. Furukawa, T. Mori, H. Ogasawara, J. Nakamura, Activating nitrogen-doped graphene oxygen reduction electrocatalysts in acidic electrolytes using hydrophobic cavities and proton-conductive Particles, *Angew. Chemie - Int. Ed.* 61 (2022), <https://doi.org/10.1002/anie.202212506>.
- [62] L. Osmieri, A.H.A. Monteverde Videla, P. Ocón, S. Specchia, Kinetics of oxygen electroreduction on me-N-C (me = fe co, cu) catalysts in acidic medium: insights on the effect of the transition metal, *J. Phys. Chem. c* 121 (2017) 17796–17817, <https://doi.org/10.1021/acs.jpcc.7b02455>.
- [63] F. Fouda-Onana, S. Bah, O. Savadogo, Palladium-copper alloys as catalysts for the oxygen reduction reaction in an acidic media I: Correlation between the ORR kinetic parameters and intrinsic physical properties of the alloys, *J. Electroanal. Chem.* 636 (2009) 1–9, <https://doi.org/10.1016/j.jelechem.2009.06.023>.
- [64] R. Guidelli, R.G. Compton, J.M. Feliu, E. Gileadi, J. Lipkowski, W. Schmickler, S. Trasatti, Defining the transfer coefficient in electrochemistry: an assessment (IUPAC technical report), *Pure Appl. Chem.* 86 (2014) 245–258, <https://doi.org/10.1515/pac-2014-5026>.
- [65] S. Treimer, A. Tang, D.C. Johnson, A consideration of the application of koutecký-Levich plots in the diagnoses of charge-transfer mechanisms at rotated disk electrodes, *Electroanalysis.* 14 (2002) 165–171, [https://doi.org/10.1002/1521-4109\(200202\)14:3<165::AID-ELAN165>3.0.CO;2-6](https://doi.org/10.1002/1521-4109(200202)14:3<165::AID-ELAN165>3.0.CO;2-6).
- [66] L. Osmieri, R. Escudero-Cid, M. Armandi, P. Ocón, A.H.A. Monteverde Videla, S. Specchia, Effects of using two transition metals in the synthesis of non-noble electrocatalysts for oxygen reduction reaction in direct methanol fuel cell, *Electrochim. Acta* 266 (2018) 220–232, <https://doi.org/10.1016/j.electacta.2018.02.036>.
- [67] R. Zhou, Y. Zheng, M. Jaroniec, S.Z. Qiao, Determination of the electron transfer number for the oxygen reduction reaction: from theory to Experiment, *ACS Catal.* 6 (2016) 4720–4728, <https://doi.org/10.1021/acscatal.6b01581>.
- [68] A. Muthukrishnan, Y. Nabee, Estimation of the inherent kinetic parameters for oxygen reduction over a pt-free cathode catalyst by resolving the quasi-four-electron reduction, *J. Phys. Chem. c* 120 (2016) 22515–22525, <https://doi.org/10.1021/acs.jpcc.6b07905>.
- [69] L. Osmieri, R. Escudero-Cid, A.H.A. Monteverde Videla, P. Ocón, S. Specchia, Application of a non-noble fe-N-C catalyst for oxygen reduction reaction in an alkaline direct ethanol fuel cell, *Renew. Energy.* 115 (2018) 226–237, <https://doi.org/10.1016/j.renene.2017.08.062>.
- [70] P. Delahay, D.R. Turner, *New Instrumental Methods in Electrochemistry* (1955), <https://doi.org/10.1149/1.2429993>.
- [71] A. Houmam, Electron transfer initiated reactions: bond formation and bond dissociation, *Chem. Rev.* 108 (2008) 2180–2237, <https://doi.org/10.1021/cr068070x>.
- [72] M. Bonchio, V. Conte, F. Di Furia, G. Modena, S. Moro, T. Carofiglio, F. Magno, P. Pastore, Correlation between one-electron reduction and oxygen-oxygen bond strength in d<sup>0</sup> transition metal peroxo complexes, *Inorg. Chem.* 32 (1993) 5797–5799, <https://doi.org/10.1021/ic00077a024>.
- [73] J. Chlistunoff, RRDE and voltammetric study of ORR on pyrolyzed fe/polyaniline catalyst. on the origins of variable tafel slopes, *J. Phys. Chem. c* 115 (2011) 6496–6507, <https://doi.org/10.1021/jp108350t>.
- [74] Z. Shi, H. Liu, K. Lee, E. Dy, J. Chlistunoff, M. Blair, P. Zelenay, J. Zhang, Z.S. Liu, Theoretical study of possible active site structures in cobalt-polypyrrole catalysts for oxygen reduction reaction, *J. Phys. Chem. c* 115 (2011) 16672–16680, <https://doi.org/10.1021/jp2027719>.
- [75] E. Laviron, General expression of the linear potential sweep voltammogram in the case of diffusionless electrochemical systems, *J. Electroanal. Chem.* 101 (1979) 19–28, [https://doi.org/10.1016/S0022-0728\(79\)80075-3](https://doi.org/10.1016/S0022-0728(79)80075-3).